Unmanned Systems, Vol. 9, No. 1 (2021) 73–86
© World Scientific Publishing Company
DOI: 10.1142/S2301385021500060

UNMANNED SYSTEMS
https://www.worldscientific.com/worldscinet/us

Un. Sys. 2021.09:73-86. Downloaded from www.worldscientific.com
by CHINESE UNIVERSITY OF HONG KONG on 12/30/20. Re-use and distribution is strictly not permitted, except for Open Access articles.

# Modeling and Control of Swing Oscillation of Underactuated Indoor Miniature Autonomous Blimps

Qiuyang Tao*, Tun Jian Tan†, Jaeseok Cha‡, Ye Yuan§, Fumin Zhang*,¶

*School of Electrical and Computer Engineering
Georgia Institute of Technology Atlanta, GA 30332, USA

†Department of Electronic and Computer Engineering
The Hong Kong University of Science and Technology
Hong Kong SAR, P. R. China

‡School of Mechanical Engineering
Georgia Institute of Technology
Atlanta, GA 30313, USA

§School of Automation
Huazhong University of Science and Technology
Wuhan, Hubei 430074, P. R. China

Swing oscillation is widely observed among indoor miniature autonomous blimps (MABs) due to their underactuated design and unique aerodynamic shape. This paper presents the modeling, identification and control system design that reduce the swing oscillation of an MAB during hovering flight. We establish a dynamic model to describe the swing motion of the MAB. The model parameters are identified from both physical measurements, computer modeling and experimental data captured during flight. A control system is designed to stabilize the swing motion with features including low latency and center-of-mass (CM) position estimation. The modeling and control methods are verified with the Georgia-Tech Miniature Autonomous Blimp (GT-MAB) during hovering flight. The experimental results show that the proposed methods can effectively reduce the swing oscillation of GT-MAB.

*Keywords*: Miniature autonomous blimp; dynamic modeling; system identification; flight control system.

US

## 1. Introduction

Indoor aerial robots are gaining increasing attention owing to their promising applications including surveillance, building exploration and search and rescue [1–4]. Human–robot interaction with indoor airborne robots is a growing research trend in recent years [5–8]. However, most existing indoor aerial platforms, such as quadcopters, have fast-spinning propellers which may cause safety concerns in human-occupied indoor environments [3,9–11]. Besides, these platforms usually have limited flight endurance [12], which restricts their applications. Lighter than air robots (LTARs) keep themselves aloft without the need for consistent motor action. Hence, LTARs are the most power efficient unmanned aerial systems [12], and their endurance can be several orders of magnitude greater than that of heavier-than-air vehicles [13]. The extended flight endurance makes LTARs well-suited to many applications that require sustained airborne presence [13, 14]. Moreover, LTARs can fly quietly owing to the reduced requirements on propulsion [15]. However, the size of LTARs is usually at the scale of a couple meters such that it can obtain sufficient amount of buoyancy [12, 16]. As a consequence, most LTARs are designed for outdoor applications instead of indoor purposes.

Received 12 October 2019; Revised 14 June 2020; Accepted 14 June 2020; Published 2 October 2020. This paper was recommended for publication in its revised form by editorial board member, Biao Wang.
Email Address: ¶*fumin@gatech.edu*

Un. Sys. 2021.09:73-86. Downloaded from www.worldscientific.com
by CHINESE UNIVERSITY OF HONG KONG on 12/30/20. Re-use and distribution is strictly not permitted, except for Open Access articles.

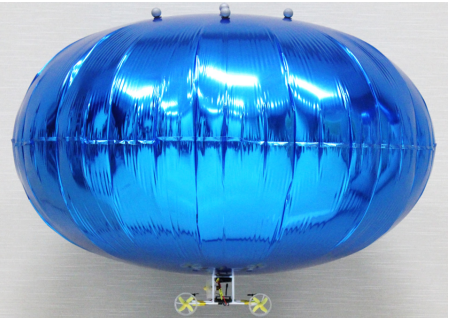

Fig. 1. GT-MAB assembly with localization markers and gondola installed at the top and the bottom of the envelope.

We develop the Georgia-Tech Miniature Autonomous Blimp (GT-MAB), a small-sized LTAR specifically designed for indoor applications [17]. Owing to the light-weight mechatronics design, the diameter of GT-MAB is only around 0.7 m while still guarantees payload capacity for devices including IMU and wireless camera [18]. The miniature size of GT-MAB ensures its mobility in indoor spaces. As shown in Fig. 1, GT-MAB is cushioned with a helium-filled envelope, making the robot safe to fly indoors, and causing no threat to human and the surroundings even with collisions. With the lifting force provided by buoyancy, GT-MAB has flight endurance for more than 2 h [19, 20]. Our previous works have investigated the dynamic model and the controller design for the translational and steering motion of GT-MAB, and developed autopilot systems that can navigate the blimp in 3D space [19, 20]. The existing modeling and control approaches successfully demonstrated their capabilities on GT-MAB, and have been adopted in many applications including environmental sampling [19] and human–robot interaction [9, 18, 20]. However, lateral and longitudinal oscillation is often observed due to the underactuated design and the unique aerodynamic shape of GT-MAB. This undesirable oscillation has impacts on certain applications of GT-MAB. The onboard sensors usually have directionality, and oscillation could cause inaccurate readings. Moreover, the quality of the video stream from the onboard camera is affected by the oscillatory movement. Mechanical gimbals can be installed on aerial robots to stabilize the sensors [21], but such a device may exceed the payload capacity of indoor miniature blimps. Besides, the oscillation consumes extra energy and might cause people to feel less comfortable interacting with the robot. Therefore, it is crucial to study the dynamic model of the swing oscillation, and design controllers to reduce this undesirable motion.

Dynamic modeling of large outdoor airships has long been studied [22], However, due to the unique design and indoor application of GT-MAB, the existing methods for outdoor airships do not apply. In contrast to conventional outdoor airships, which usually have cigar-shaped envelope and tail fins, GT-MAB features a unique tailless “saucer-shaped” envelope, to obtain adequate buoyancy, omnidirectional mobility and outstanding safety in indoor spaces. As a trade-off, existing analytical methods for modeling the conventional cigar-shaped airships, i.e. [23], can hardly be applied to GT-MAB. Moreover, as shown in Fig. 1, there is folding on the envelope of GT-MAB. The nonsmooth surface makes it hard to accurately construct model and perform computational fluid dynamics (CFD) simulations such as [24, 25]. Besides, hovering and slow-flying are the most common operating scenarios for indoor blimps, while outdoor airships are usually designed for cruising. As a consequence, wind tunnel tests, i.e. [26, 27], are not applicable due to the low-speed nature of GT-MAB. In summary, the nonconventional shape, nonsmooth envelope and slow-flying nature of GT-MAB are the major difficulties in modeling the swing motion of GT-MAB.

Due to the limitations including light-weight mechatronics, miniature indoor blimps are not widely available until recently. Only a few projects address the modeling of the conventional cigar-shaped indoor blimps with sizes slightly larger than the saucer-shaped GT-MAB. The existing approaches for modeling the dynamics of indoor blimps can be categorized into two groups, analytical and data-driven. The analytical methods investigate the aerodynamics from the specific shape of the blimp [28]. The work [29] presented the dynamics of a cigar-shaped indoor blimp, and simplified the model to separate the translational and steering motion. The model was then further reduced to only considering the horizontal and steering motion for the convenience of studying the control strategy under wind disturbance. However, identification of the parameters, such as the viscous coefficient, was not discussed. The work [30] derived the 6-DOF mathematical model of a cigar-shaped indoor blimp. The pitch and roll angles were assumed to be small, and the model was simplified by removing the roll and pitch dynamics. Authors of [28] modeled the 6-DOF dynamics of an indoor blimp, and developed a simulator based on the model. Parameters of the dynamic model were analyzed given the geometry of the envelope. Unfortunately, all these works [28–30] focus on modeling indoor blimps with cigar-shaped envelope. Since the analytical methods may only be valid for a specific class of envelope shapes [31], the existing analytical methods for modeling the traditional cigar-shaped blimps cannot be easily applied to saucer-shaped blimps such as GT-MAB. Data-driven approaches discover the dynamics from data measurements [32]. The work [32] simplified the dynamical equation of an indoor blimp along its vertical axis, and then identified the model parameters from the step response of the vertical motion. The parameters of upward and downward motion were identified separately due to the asymmetric dynamics

Un. Sys. 2021.09:73-86. Downloaded from www.worldscientific.com
by CHINESE UNIVERSITY OF HONG KONG on 12/30/20. Re-use and distribution is strictly not permitted, except for Open Access articles.

of the vertical motion. Unfortunately, only vertical motion was considered in this work. Our previous work [20] simplified the dynamic model of GT-MAB into decoupled translational and steering motion. The parameters of each decoupled movement were identified separately. Similarly, the recent work [4] simplified and identified the model of an indoor blimp as decoupled altitude and planar movements. However, the roll and pitch motions were not considered in these works [4, 20]. To the best of our knowledge, our recent work [33] is the only literature addressing the swing oscillation of saucer-shaped indoor blimps among the existing efforts on developing this type of robot such as [8, 34, 35]. However, controller design on reducing the swing oscillation was not presented in [33].

All onboard electronics of GT-MAB, including the thrusters, are installed on one single 3D printed gondola mounted underneath the envelope. This configuration reduces weight, ensures alignment between thrusters and enhances the durability of the blimp. However, this underactuated thruster configuration also causes undesired pitching or rolling torque once the motors are on. This disturbance shows a more significant impact on the roll and pitch motion of GT-MAB when more powerful thrusters are installed for better maneuverability and flyability against airflow. Moreover, similar to marine vehicles [36, 37], GT-MAB usually operates under various disturbances such as indoor air ventilation. The environmental disturbances also introduce undesired swing motion to the blimp. Besides, most MABs require external localization systems to fly inside the GPS-denied indoor environment. These systems usually incorporate multiple ceiling-mounted infrared cameras to track the retroreflective markers installed on the robots. The localization markers are usually installed at the top of the envelope for the best visibility to the cameras. The measurement from the localization systems is the pose of the markers. The marker position has constant offset above the center of mass (CM) of GT-MAB and is used to represent the position of the blimp when there is negligible roll or pitch angle. However, the tracker position becomes fluctuated when GT-MAB is swinging, which further aggregates the swing oscillation. Therefore, the CM position of GT-MAB needs to be estimated from the identified swing dynamic model, and incorporated in controller design. Moreover, the external localization system requires a ground station computer to interface with the cameras and to compute the pose of GT-MAB. Other computationally intensive tasks, such as object detection, are also implemented on the ground station computer to save payload and energy. Therefore, wireless communication is required to exchange data between the ground station and onboard electronics of GT-MAB. However, as reported in work [32], control system latency of indoor blimp with external localization device and off-board computing is around 0.2–0.4 s. The latency is acceptable to control the relatively slow translational and steering motion of GT-MAB, but cannot satisfy the needs for regulating the fast swing oscillation. As a summary, the main difficulties in reducing the swing motion of GT-MAB are its unique underactuated design, fluctuated position measurement, and latency in the control system.

Flight controllers for the existing indoor miniature blimps can be categorized into two groups based on whether a dynamic model is required. Without the dynamic model, the work [38] compared PID and fuzzy logic algorithms for altitude control, and presented a fuzzy logic controller for collision avoidance. Authors of the work [39] presented a biologically based flight controller with visual information from two camera inputs. PID controllers were designed in [16, 40, 41] for motion control and landing. Cooperative control of multiple neural networks is reported in [42] for the robustness with mechanical failures. The work [43] presented a behavior-based navigation system for an indoor blimp. The other portion of the existing literature on controller design incorporates the dynamic model of the blimp. The work [29] studied the control strategy under wind disturbance, and verified the proposed controller design by simulation. Authors of [30] presented both modeling and controller design of a solar-powered indoor blimp. The experimental results showed that the blimp can successfully track a straight path in 3D space. The work [28] designed neuromorphic controllers, and trained the neural network using a simulator with identified dynamic model. The trained controller was then transferred on the physical blimp, and resulted in a very similar behavior with the simulated one. The works [32, 44, 45] designed a predictor-based controller to compensate for the system latency. Experimental results showed the controller can keep the blimp at the desired altitude. However, only the altitude-related modeling and control was considered in [32, 44, 45]. Our previous work [20] designed controllers for the translational and steering motion of GT-MAB, and designed a waypoint following controller by combining a set of motion primitives. The flight controllers of GT-MAB were also validated by supporting the multi-agent path-planning method developed in the work [46]. Similarly, the recent work [4] designed flight controllers for the decoupled vertical and planar motions of an indoor blimp. Moreover, PD controllers were implemented for the motion primitives of MABs with tilting [10] and quadcopter-like [47] actuator configurations. However, to the best of our knowledge, there is no existing controller design addressing the swing oscillation of saucer-shaped MABs.

In this paper, we extend our previous efforts on modeling the swing motion of GT-MAB by designing a flight control system that reduces this undesired oscillation. The system addresses the difficulties in reducing the swing motion of

Un. Sys. 2021.09:73-86. Downloaded from www.worldscientific.com
by CHINESE UNIVERSITY OF HONG KONG on 12/30/20. Re-use and distribution is strictly not permitted, except for Open Access articles.

GT-MAB including the underactuated design, fluctuated position measurement, and latency in the control system. Feedback controllers are designed based on the identified swing dynamics to regulate the roll and pitch motion of GT-MAB. The CM position of GT-MAB is estimated from the identified model parameters and the pose of the blimp. The CM position is then incorporated in the controller design to replace the tracker position for reduced fluctuation. The latency of the control system is improved through better mechatronics design and software implementation. Experiments are conducted to verify the effectiveness of the proposed control system. The experimental results show that the swing oscillation of GT-MAB can be effectively reduced. The swing oscillation is a common problem among indoor miniature blimps. Due to the small size and payload constraints, the bottom-heavy underactuated design is widely adopted by many indoor MABs such as [34, 35]. As a result, the undesired swing oscillation is also inevitable for most indoor MABs besides GT-MAB. Therefore, the proposed methods could be applied to other indoor MABs.

This paper is organized as follows: in Sec. 2, the motion model of GT-MAB is established to describe the swing oscillation. In Sec. 3, the parameters of the swing dynamics are identified, linearized, and validated for controller design. In Sec. 4, a flight control system is designed and experimentally validated to reduce the swing oscillation. In Sec. 5, we draw the conclusion and discuss future work.

## 2. Motion Model for a Miniature Blimp

In this section, we first present the kinematics and coordinate frame definitions. Then the dynamic model of a miniature indoor blimp, GT-MAB, is established and simplified to describe its swing oscillation during the hovering flight.

### 2.1. *Kinematics and coordinate frames*

Figure 2 shows the definition of the inertial frame, body frame, and the coordinates of the motion capture system. The inertial frame is denoted as $O_I - X_I Y_I Z_I$ with axis $Z_I$ pointing downward. The body frame $O_B - X_B Y_B Z_B$ is established at the center of mass of GT-MAB. We use an optical localization system (OptiTrack) to track the pose of the reflective markers on GT-MAB at millimeter level accuracy. The coordinate system of the motion tracking system is defined as $O_L - X_L Y_L Z_L$ with Y-up convention. For convenience, we let $O_L$ coincide with $O_I$, and $O_L X_L$ parallel to $O_I X_I$. The localization markers are installed at the top of the envelope for the best visibility to the motion tracking system. The pose of the

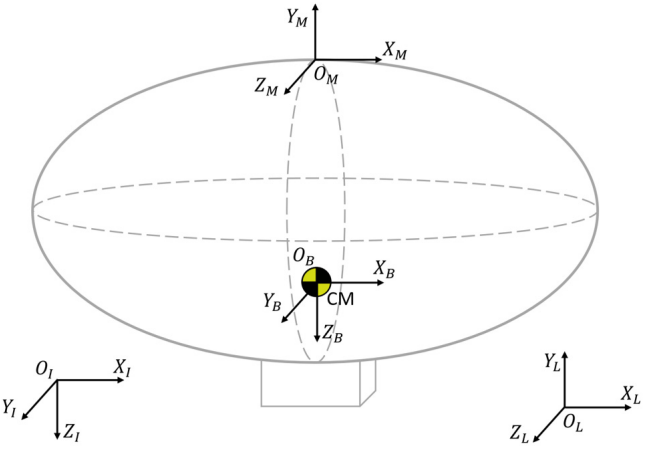


Fig. 2. Illustration of the coordinate frames.

markers in the localization system is denoted as $O_M - X_M Y_M Z_M$. Given the fact that $O_M - X_M Y_M Z_M$ is usually calibrated to align with $O_B - X_L Y_L Z_L$ when GT-MAB is leveled, we can assume that the plane $X_M Z_M$ is parallel to $X_B Y_B$, and $O_M X_M$ is parallel to $O_B X_B$.

Let $\boldsymbol{\eta_1} = [x, y, z]^\top$ and $\boldsymbol{\eta_2} = [\phi, \theta, \psi]^\top$ represent position and orientation of GT-MAB in inertial frame. The pose of GT-MAB is denoted as $\boldsymbol{\eta} = [\boldsymbol{\eta_1}, \boldsymbol{\eta_2}]^\top$. Linear and angular velocity of GT-MAB in the body frame is described by $\boldsymbol{\nu} = [\boldsymbol{V}, \boldsymbol{\Omega}]^\top$, where $\boldsymbol{V} = [u, v, w]^\top$ and $\boldsymbol{\Omega} = [p, q, r]^\top$. According to the work [13], relationship between the velocities in different coordinate frames is given by

$$\begin{bmatrix} \dot{\boldsymbol{\eta}}_1 \\ \dot{\boldsymbol{\eta}}_2 \end{bmatrix} = \begin{bmatrix} \boldsymbol{R}(\boldsymbol{\eta}_2) & 0_{3\times3} \\ 0_{3\times3} & \boldsymbol{J}(\boldsymbol{\eta}_2) \end{bmatrix} \begin{bmatrix} \boldsymbol{V} \\ \boldsymbol{\Omega} \end{bmatrix}, \tag{1}$$

where $\boldsymbol{R}(\boldsymbol{\eta_2})$ is the rotation matrix. Using the simplified notation $c\cdot = \cos(\cdot)$ and $s\cdot = \sin(\cdot)$, $\boldsymbol{R}(\boldsymbol{\eta_2})$ has the form of

$$\boldsymbol{R}(\boldsymbol{\eta_2}) = \begin{bmatrix} c\psi c\theta & -s\psi c\phi + c\psi s\theta s\phi & s\psi s\phi + c\psi s\theta c\phi \\ s\psi c\theta & c\psi c\phi + s\psi s\theta s\phi & -c\psi s\phi + s\psi s\theta c\phi \\ -s\theta & c\theta s\phi & c\theta c\phi \end{bmatrix}. \tag{2}$$

The term $\boldsymbol{J}(\boldsymbol{\eta_2})$ in Eq. (1) can be represented as follows:

$$\begin{aligned} \boldsymbol{J}(\boldsymbol{\eta_2}) &= \begin{bmatrix} 1 & 0 & -s\theta \\ 0 & c\phi & s\phi c\theta \\ 0 & -s\phi & c\phi c\theta \end{bmatrix}^{-1} \\ &= \begin{bmatrix} 1 & s\phi\tan\theta & c\phi\tan\theta \\ 0 & c\phi & -s\phi \\ 0 & s\phi/c\theta & c\phi/c\theta \end{bmatrix}. \end{aligned} \tag{3}$$

Un. Sys. 2021.09:73-86. Downloaded from www.worldscientific.com
by CHINESE UNIVERSITY OF HONG KONG on 12/30/20. Re-use and distribution is strictly not permitted, except for Open Access articles.

### 2.2. *Dynamic model of GT-MAB*

From our previous works [20, 33], the generic 6-DOF dynamic model of GT-MAB is given as follows:

$$m(\dot{\boldsymbol{V}} + \boldsymbol{\Omega} \times \boldsymbol{V}) = \boldsymbol{F} + \boldsymbol{f}, \tag{4}$$
$$\boldsymbol{I}\dot{\boldsymbol{\Omega}} + \boldsymbol{\Omega} \times (\boldsymbol{I}\boldsymbol{\Omega}) = \boldsymbol{M} + \boldsymbol{\tau},$$

where $m$ is the total mass of the blimp, including the mass of the helium gas inside the envelope and the added mass. The terms $\boldsymbol{f} = [f_x, f_y, f_z]^\top$ and $\boldsymbol{\tau} = [\tau_x, \tau_y, \tau_z]^\top$ are linear forces and moments generated by the thrusters. Let $\boldsymbol{F} = [F_x, F_y, F_z]^\top$ and $\boldsymbol{M} = [M_x, M_y, M_z]^\top$ represent the sum of forces and moments due to gravity, buoyancy, and other aerodynamic forces acting on the blimp. The terms $\boldsymbol{f}$, $\boldsymbol{F}$, $\boldsymbol{\tau}$ and $\boldsymbol{M}$ are all defined in the body-fixed frame. The symbol $\boldsymbol{I}$ represents the inertia matrix of GT-MAB about CM, which is the sum of rigid-body inertia and added inertia:

$$\boldsymbol{I} = \begin{bmatrix} I_x & -I_{xy} & -I_{xz} \\ -I_{yx} & I_y & -I_{yz} \\ -I_{zx} & -I_{zy} & I_z \end{bmatrix}. \tag{5}$$

Owing to the symmetric design of GT-MAB, namely CM of the robot is on $Z_B$ axis, the inertia matrix can be simplified as diagonal with $I_x = I_y$. Similarly, the term $\boldsymbol{\Omega} \times (\boldsymbol{I}\boldsymbol{\Omega})$ in Eq. (4) can be neglected [20]. Therefore, the rotational motion of GT-MAB can be simplified as follows:

$$\boldsymbol{I}\dot{\boldsymbol{\Omega}} = \boldsymbol{M} + \boldsymbol{\tau}. \tag{6}$$

Thus, the swing-related pitch and roll motion of GT-MAB can be decoupled as follows:

$$I_x\dot{p} = M_x + \tau_x$$
$$I_y\dot{q} = M_y + \tau_y. \tag{7}$$

### 2.3. *Dynamic model of pitching motion*

As discussed in Sec. 2.2, the pitch and roll dynamics of GT-MAB are decoupled and almost identical. Therefore, we only focus on the pitch motion in dynamic modeling and identification. Hence, the attitude and angular velocity are assumed to be $\boldsymbol{\eta_2} = [0, \theta, 0]^\top$ and $\boldsymbol{\Omega} = [0, q, 0]^\top = [0, \dot{\theta}, 0]^\top$. For simplicity, we assume CM is the pivot of the pitching oscillation. Therefore, the translational velocity at CM is zero when GT-MAB is hovering. Owing to the consistent CM position, we neglect the added mass effect for the translational motion. Thus, we assume the total mass of GT-MAB, $m$, equals to the rigid-body mass of the blimp.

Figure 3 demonstrates the major forces and moments while GT-MAB is pitching. The pair of forces, $F_B$ and $F_G$, are the buoyancy and gravitational force at the center of volume (CV) and CM. The distance between CV and CM is denoted as $d_{\mathrm{VM}}$. Due to this bottom-heavy design, there is a gravitational restoring torque, $M_G$, which stabilizes the blimp while it is pitching. $f(u)$ represents the motor thrust in $X_B$ direction, where $u$ is the controller output for the corresponding thruster. Since the thrusters are installed beneath the envelope, the motor-induced torque about CM, $\tau$, will be generated. The rotational inertia and air damping moment about CM are denoted as $I_{\mathrm{CM}}$ and $M_d$ separately. Therefore, the pitching motion of GT-MAB can be described as follows:

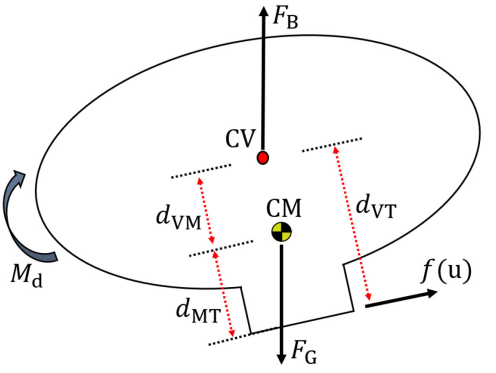


Fig. 3. Side view of GT-MAB. Forces and moments that contribute to the pitching oscillation are annotated on the plot.

$$I_{\mathrm{CM}}\dot{q} = I_{\mathrm{CM}}\ddot{\theta} = M_d + M_G + \tau. \tag{8}$$

The aerodynamic damping term, $M_d$, can be assumed to be linear to angular velocity $\dot{\theta}$ for low-speed indoor blimps [27]. Denote $b$ as the damping coefficient, and $M_d$ can be found as follows:

$$M_d = -bq = -b\dot{\theta}. \tag{9}$$

The gravitational restoring torque, $M_G$, stabilizes the blimp given that the CM is below the center of buoyancy. This stabilization moment, $M_G$, can be represented as follows:

$$M_G = -F_B d_{\mathrm{VM}} \sin(\theta). \tag{10}$$

Due to the displacement between the thrusters and the pitching pivot, the thruster-induced torque $\tau$ is inevitable when motors are turned on. The torque $\tau$ can be found as follows:

$$\tau = d_{\mathrm{MT}} f(u). \tag{11}$$

Therefore, the pitching dynamics of GT-MAB described in Eq. (8) can be expanded as follows:

$$I_{\mathrm{CM}}\ddot{\theta} = -b\dot{\theta} - F_{\mathrm{B}} d_{\mathrm{VM}} \sin(\theta) + d_{\mathrm{MT}} f(u). \tag{12}$$

As illustrated in Fig. 3, the term $d_{\mathrm{MT}}$ can be written as $d_{\mathrm{MT}} = d_{\mathrm{VT}} - d_{\mathrm{VM}}$, where $d_{\mathrm{VT}}$ is a constant parameter from the dimension measurements in Sec. 3.1. GT-MAB is

Un. Sys. 2021.09:73-86. Downloaded from www.worldscientific.com
by CHINESE UNIVERSITY OF HONG KONG on 12/30/20. Re-use and distribution is strictly not permitted, except for Open Access articles.

neutrally ballasted prior to each flight, thus we can assume that the total buoyancy $F_B$ is equal to the total gravitational force, hence $F_B = F_G = mg$, where $g$ is gravitational constant. Therefore, the pitching dynamics in Eq. (12) can be written as follows:

$$I_{CM}\ddot{\theta} = -b\dot{\theta} - d_{VM}\sin(\theta)mg - (d_{VT} - d_{VM})f(u). \quad (13)$$

### 2.4. *Gray box model*

The terms $d_{VM}$, $d_{VT}$, $m$, and $f(u)$ in Eq. (13) can be calculated or measured with relatively good accuracy. However, the air damping coefficient $b$, and the moment of inertia $I_{CM}$, cannot be easily estimated due to the complex aerodynamics effects and the unconventional shape of GT-MAB. Therefore, a gray box model is constructed to represent the pitching dynamics of GT-MAB, where the model structure is explicitly specified, and the parameters are partially known. Denote the angle and angular rate of GT-MAB's pitching motion as $\boldsymbol{x} = [\theta, \dot{\theta}]^\top$, and the gray box model can be represented as follows:

$$\begin{aligned} \dot{x_1} &= x_2 \\ \dot{x_2} &= [-bx_2 - mgd_{VM}\sin(x_1) + (d_{VT} - d_{VM})f(u)]/I_{CM}. \end{aligned} \quad (14)$$

## 3. Parameter Identification

This section discusses the parameter identification of the gray box model that describes the pitching dynamics of GT-MAB. The model with identified parameters is then linearized for controller design and validated with experimental data.

### 3.1. *The parameter $d_{VT}$*

$d_{VT}$ is the distance between the CV and the motor thrust force $f$, as demonstrated in Fig. 3. In contrast to large outdoor airships which usually adjust their buoyancy by changing the volume of air and helium, GT-MAB uses thrusters to adjust its altitude to reduce the size and improve maneuverability. Therefore, the dimension of GT-MAB is consistent, and can be considered as a rigid body when inflated. Owing to this, $d_{VT}$ is a constant parameter and can be calculated as follows:

$$d_{VT} = H_{ENV}/2 + H_{GON}, \quad (15)$$

where $H_{ENV}$ and $H_{GON}$ are the thickness of the envelope and the height of the gondola, as illustrated in Fig. 4. With the measurement $H_{ENV} = 0.44\,\text{m}$ and $H_{GON} = 0.04\,\text{m}$, we have $d_{VT} = 0.26\,\text{m}$.

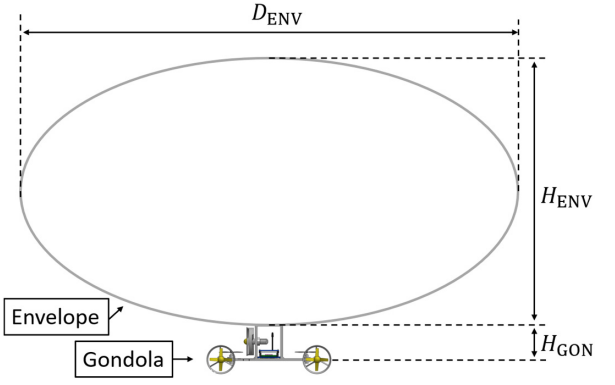


Fig. 4. Dimension of the envelope and the gondola of GT-MAB.

### 3.2. *The thrust $f(u)$*

$f(u)$ represents the mapping between the motor thrust and the input command. The command $u \in [-1, 1]$ represents the duty circle that controls the DC motor of GT-MAB. Positive $u$ will result in the motor thrusting in $X_B$ direction, while a negative value will generate force oppositely. Neglecting the resistance of the electronics such as H-bridge, we can approximate the voltage applied to the motor as follows:

$$V_{motor} = V_{batt} \cdot u, \quad (16)$$

where $V_{batt}$ is the voltage of the battery, which can be measured by the circuitry on GT-MAB. Similar to the work [27], we measure the motor thrust with a high-accuracy scale. The relationship between the motor thrust and the applied voltage can be seen in Fig. 5.

### 3.3. *The total mass $m$*

The total mass of GT-MAB, $m$, is hard to be directly measured since the Helium gas inside the envelope cannot be easily gauged. Instead, by measuring the lifting force

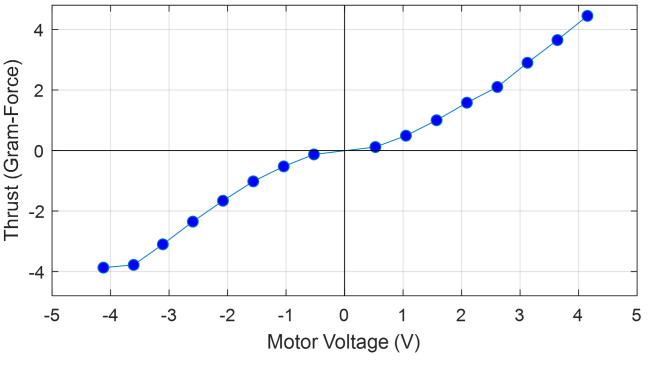


Fig. 5. Motor thrust in $X_B$ direction, versus the voltage applied on the motors, $V_{motor}$.

Un. Sys. 2021.09:73-86. Downloaded from www.worldscientific.com
by CHINESE UNIVERSITY OF HONG KONG on 12/30/20. Re-use and distribution is strictly not permitted, except for Open Access articles.

provided by the envelope, we can derive the total buoyancy of GT-MAB, and therefore find the total mass of the vehicle. Let $F_{\text{lift}}$ be the lifting force provided by the envelope, which is equal to the total buoyancy $F_B$ minus the gravitational forces of the Helium gas and the deflated envelope. Moreover, since GT-MAB is neutrally buoyant, $F_{\text{lift}}$ equals to the gravitational force of all the components that are attached on the envelope, thus the gondola assembly, the ballast weight, and the localization trackers. Therefore, $F_B$ and $F_{\text{lift}}$ can be represented as follows:

$$\begin{aligned} F_{\text{lift}} &= F_B - (m_{\text{env}} + m_{\text{He}})g \\ &= (m_{\text{gon}} + m_{\text{mkr}} + m_{\text{blst}})g, \end{aligned} \tag{17}$$

$$\begin{aligned} F_{\text{B}} &= (m_{\text{env}} + m_{He})g \\ &\quad + (m_{\text{gon}} + m_{\text{mkr}} + m_{\text{blst}})g, \end{aligned} \tag{18}$$

where $m_{\text{env}}$, $m_{\text{He}}$, $m_{\text{gon}}$, $m_{\text{mkr}}$, $m_{\text{blst}}$ are the mass of the deflated envelope, helium gas, gondola assembly, localization makers and the ballast weight to keep GT-MAB neutrally buoyant.

According to Archimedes' principle, and assuming the envelope dominates the volume of GT-MAB, we can find that the total buoyancy $F_B$ is equal to the weight of air that the envelope displaces. Then, Eq. (18) for $F_B$ can be written as follows:

$$\begin{aligned} F_B &= \rho_{\text{air}} V_{\text{env}} g \\ &= (m_{\text{env}} + m_{\text{He}})g \\ &\quad + (m_{\text{gon}} + m_{\text{mkr}} + m_{\text{blst}})g, \end{aligned} \tag{19}$$

where $\rho_{\text{air}}$ and $V_{\text{env}}$ are the density of air and the volume of the envelope. Given that the mass of the helium gas is

$$m_{\text{He}} = \rho_{\text{He}} V_{\text{He}} = \rho_{\text{He}} V_{\text{env}}, \tag{20}$$

the volume of the envelope can be calculated as follows:

$$V_{\text{env}} = \frac{m_{\text{gon}} + m_{\text{mkr}} + m_{\text{blst}} + m_{\text{env}}}{\rho_{\text{air}} - \rho_{\text{He}}}. \tag{21}$$

Assuming the temperature of the indoor environment is around 300 K (26.85 °C), density of both helium and air is known as $\rho_{\text{He}} = 0.164\,\text{kg/m}^3$ and $\rho_{\text{air}} = 1.161\,\text{kg/m}^3$. With the total mass of the four components in Eq. (21) measured as 107.24 g, the overall mass of GT-MAB, $m$, can be calculated as follows:

$$m = \rho_{\text{air}} V_{\text{env}} = 0.1249\,\text{kg}. \tag{22}$$

### 3.4. $d_{\text{VM}}$ and initial approximation of $I_{\text{CM}}$

With the mass of all components of GT-MAB measured and calculated in previous sections, we use CAD software to calculate the position of the CM, namely $d_{\text{VM}}$, and the rough estimation of the moment of inertia, $I_{\text{CM}}$. The estimated $I_{\text{CM}}$ will be used as the initial approximation for the system identification experiments in Sec. 3.5.

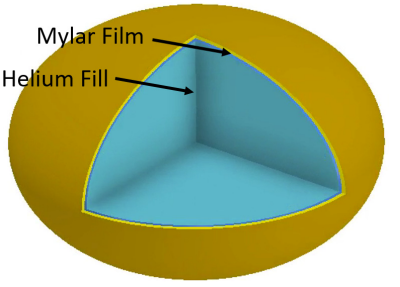


Fig. 6. CAD model of the helium-filled envelope.

As illustrated in Fig. 6, the envelope of GT-MAB is modeled as an ellipsoid in the CAD software. From work [48], dimension of the inflated envelope can be calculated by its deflated radius as follows:

$$\begin{aligned} r_{\text{in}} &\approx 0.7627 r_{\text{de}}, \\ \tau_{\text{in}} &\approx 0.9139 r_{\text{de}}, \end{aligned} \tag{23}$$

where $r_{\text{de}}$ is the radius of the deflated envelope, and $r_{\text{in}}$ and $\tau_{\text{in}}$ are the radius and thickness of the envelope when inflated. Therefore, the ellipsoid CAD model with dimension $r_{\text{in}}$ and $\tau_{\text{in}}$ is constructed with measurement $r_{\text{de}} = 0.457$ m. With Autodesk Inventor software [49], we found that $d_{\text{VM}} = 0.0971$ m and $I_{\text{CM}} = 0.00371\,\text{kg} \cdot \text{m}^2$.

### 3.5. The parameters $I_{\text{CM}}$ and $b$

Now, $I_{\text{CM}}$ and $b$ are the only two unknown parameters in the gray box model described in Eq. (14). A series of system identification experiments are designed to obtain these parameters. GT-MAB is released with initial pitch angle $\theta_0$, and the motion capture system (OptiTrack) logs the free response of the pitching oscillation. The experiment is repeated eight times with different initial angle $\theta_0$. The first seven datasets are used for identifying the parameters and the last one is for validation.

As listed in Table 1, seven $I_{\text{CM}}$ and $b$ pairs are identified from the first seven datasets with MATLAB System Identification

Table 1. Parameters identified from the experimental datasets.

| Dataset | $I_{\text{CM}}$ | $b$ | NRMSE Fit % |
|---|---|---|---|
| Dataset 1 | 0.005782 | 0.000838 | 82.16 |
| Dataset 2 | 0.005847 | 0.000978 | 85.45 |
| Dataset 3 | 0.005835 | 0.000940 | 84.29 |
| Dataset 4 | 0.005828 | 0.001140 | 85.20 |
| Dataset 5 | 0.005851 | 0.001083 | 87.26 |
| Dataset 6 | 0.005750 | 0.001025 | 77.80 |
| Dataset 7 | 0.005855 | 0.000857 | 85.21 |
| Mean | 0.005821 | 0.000980 | 83.91 |

Un. Sys. 2021.09:73-86. Downloaded from www.worldscientific.com
by CHINESE UNIVERSITY OF HONG KONG on 12/30/20. Re-use and distribution is strictly not permitted, except for Open Access articles.

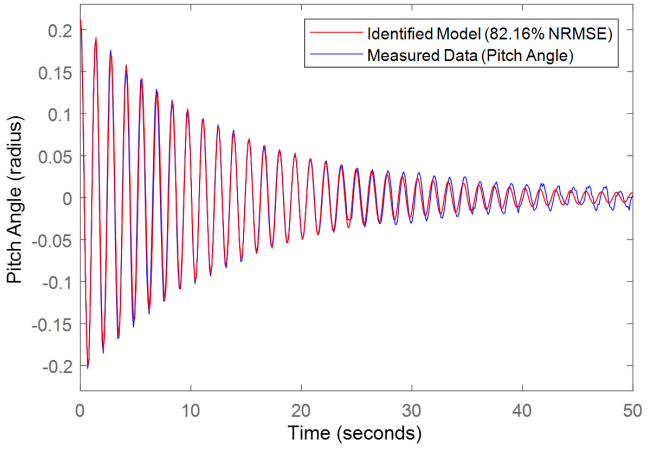


Fig. 7. Measured pitching oscillation and the simulated response with the identified parameters from dataset 1.

Toolbox [50]. Figure 7 demonstrates both the logged pitch angle and the simulated response with the identified parameters from the first dataset. The fitting between the measured and modeled system is quantified as normalized root-mean-square error (NRMSE). The final estimations of $I_{CM}$ and $b$ are found as the average of the seven identified results in Table 1, which are $I_{CM} = 0.005821\,\text{kg} \cdot \text{m}^2$ and $b = 0.000980\,\text{N} \cdot \text{m} \cdot \text{s/rad}$.

### 3.6. *Model linearization and validation*

Table 2 summarizes the parameters of the dynamic model obtained from the previous sections. Therefore, the pitching dynamic model of GT-MAB in Eq. (13) can be represented as follows:

$$\ddot{\theta} = -20.4284\sin(\theta) - 0.1684\dot{\theta} + 27.9933f(u). \quad (24)$$

The identified model is then linearized around $\theta = \dot{\theta} = 0$ for controller design. The state-space representation of the linearized model can be written as follows:

$$\begin{bmatrix} \dot{\theta} \\ \ddot{\theta} \end{bmatrix} = \begin{bmatrix} 0 & 1 \\ -20.4284 & -0.1684 \end{bmatrix} \begin{bmatrix} \theta \\ \dot{\theta} \end{bmatrix} + \begin{bmatrix} 0 \\ 27.9933 \end{bmatrix} f(u). \quad (25)$$

Table 2. Parameters of GT-MABs pitching dynamic model.

| Parameters | Value |
|---|---|
| $g$ | $9.81\,\text{m/s}^2$ |
| $I_{CM}$ | $0.005821\,\text{kg} \cdot \text{m}^2$ |
| $b$ | $0.000980\,\text{N} \cdot \text{m} \cdot \text{s/rad}$ |
| $m_{ASM}$ | $0.1249\,\text{kg}$ |
| $d_{VT}$ | $0.26\,\text{m}$ |
| $d_{VM}$ | $0.097051\,\text{m}$ |

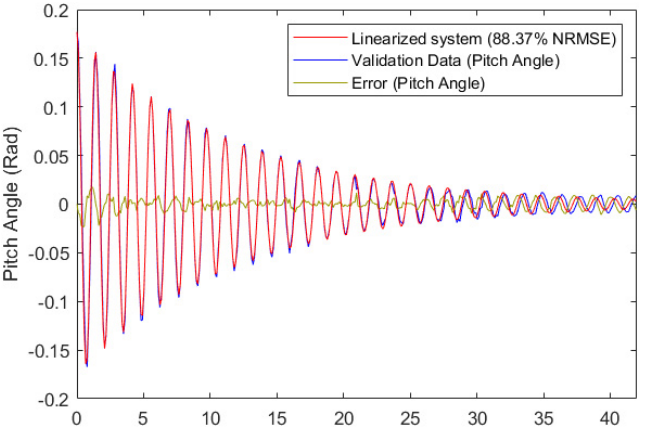


Fig. 8. Measured pitching oscillation from the validation dataset and the simulated response with the linearized dynamic model.

This linearized model is compared with the eighth dataset discussed in Sec. 3.5 for validation. The linearized model has a satisfying 88.37% NRMSE fit with the validation data, which can be seen in Fig. 8.

## 4. Flight Control System

This section presents the flight control system that stabilizes the swing motion of GT-MAB. As discussed in Sec. 1, the underactuated design, fluctuated position measurement, and control system latency are the major difficulties in stabilizing the swing oscillation of GT-MAB. In this section, we first discuss the approaches to reduce the control system latency. Then, CM position of GT-MAB is estimated for less fluctuated position measurement. Next, feedback controllers are designed and experimentally validated to reduce the swing oscillation of GT-MAB during hovering flight.

### 4.1. *System overview*

Figure 9 demonstrates the overall setup of the flight control system. The pose of GT-MAB is estimated by tracking the localization markers on top of the envelope. A ground station computer interfaces the motion capture system, and runs the flight control software. The control commands are transmitted to GT-MAB via wireless communication, and

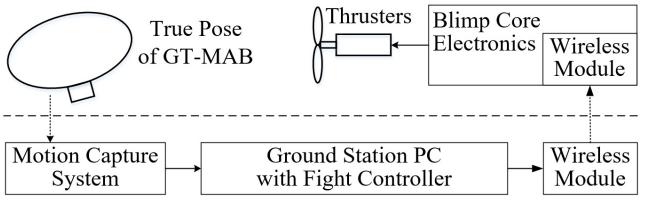


Fig. 9. Overview of GT-MABs flight control system.

Un. Sys. 2021.09:73-86. Downloaded from www.worldscientific.com
by CHINESE UNIVERSITY OF HONG KONG on 12/30/20. Re-use and distribution is strictly not permitted, except for Open Access articles.

the onboard electronics of the blimp drive the thrusters once a command is received.

### 4.2. *System latency reduction*

The fast dynamics of the swing motion requires low latency from the flight control system. We reduce the latency by implementing the flight controller software with lower-level programming language, minimizing the response time of GT-MAB's onboard electronics and firmware, and enhancing the wireless communication. Owing to the efforts on latency reduction, the update rate of the flight controller is improved to 120 Hz. As shown in Fig. 10, an experiment is designed to measure the delay in the control loop. We use a rotational plate with markers to emulate the attitude of GT-MAB during swing oscillation. By comparing the rotation angle from the rotary encoder, and the voltage applied on the thruster, we found the latency of the control system is around 30.5 ms. Compared to the period of the pitching oscillation from Fig. 7, which is approximately 1.3 s, the control system latency can be neglected.

To further reduce the response time of GT-MAB, coreless DC motors are chosen for its low rotor inertia. To evaluate the response time of the thrusters, we establish a second-order model that is simplified from work [51].

$$\begin{bmatrix} \dot{\Phi} \\ \dot{\omega} \end{bmatrix} = \begin{bmatrix} 0 & 1 \\ 0 & -1/\tau \end{bmatrix} \begin{bmatrix} \Phi \\ \omega \end{bmatrix} + \begin{bmatrix} 0 \\ \beta/\tau \end{bmatrix} V_{\text{motor}}, \tag{26}$$

where $\Phi$ and $\omega$ represents the shaft angle and angular velocity of the thruster. The terminal voltage on the motor is denoted as $V_{\text{motor}}$. $\tau$ and $\beta$ are time constant and static gain that characterize the motor response. With the experimental setup shown in Fig. 11, the step response of the thruster is collected. We fit the DC motor model to the measured response, and obtain the time constant $\tau = 28$ ms. Compared to the period of the pitching oscillation, which is around 1.3 s, the motor response time can be neglected.

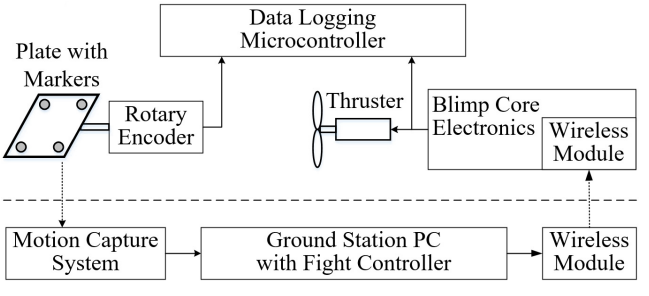


Fig. 10. Experimental setup for measuring the latency of the control system.

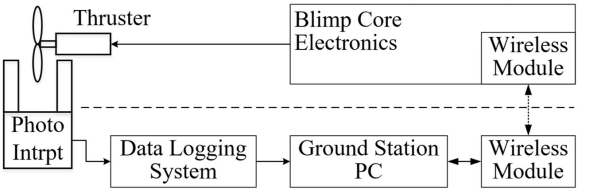


Fig. 11. Experimental setup for measuring the thruster response of GT-MAB. A photo interrupter measures the angular velocity of the thruster without contacting the motor shaft.

### 4.3. *Center-of-mass position estimation*

As shown in Fig. 12, the localization markers are placed at the top of GT-MAB for better visibility to the motion tracking cameras. However, due to the displacement between $O_M$ and CM, the position measurement of the markers has large fluctuation while GT-MAB is swinging.

With identified parameters from Sec. 3, position of CM can be estimated from the pose measurement of the localization markers. We define the vector ${}^{B}p_{\text{CM}}$ to represent the position of CM in blimp's body frame. Given the fact that $O_M$ is usually on $Z_B$ axis, ${}^{\text{B}}\boldsymbol{p}_{\text{CM}}$ can be simplified as follows:

$${}^{B}\boldsymbol{p}_{\text{CM}} = [0, 0, -d_{\text{VM}}]^{\top}, \tag{27}$$

where $d_{\text{VM}}$ is the distance between CV and CM identified in Sec. 3.1.

Since the only measurement from the motion tracking system is the pose of $O_M X_M Y_M Z_M$ in $O_L X_L Y_L Z_L$, a series of coordinate transformations are required to find the CM position in the inertial frame. We begin with representing the vector ${}^{B}\boldsymbol{p}_{\text{CM}}$ in $O_M X_M Y_M Z_M$:

$${}^{M}\boldsymbol{p}_{\text{CM}} = {}^{M}_{B}\boldsymbol{R}\,{}^{B}\boldsymbol{p}_{\text{CM}} + {}^{M}_{B}\boldsymbol{q}, \tag{28}$$

where ${}^{M}_{B}\boldsymbol{R}$ is the rotation matrix between $O_B X_B Y_B Z_B$ and $O_M X_M Y_M Z_M$, and ${}^{M}_{B}\boldsymbol{q}$ is the position of $O_B$ in $O_M X_M Y_M Z_M$.

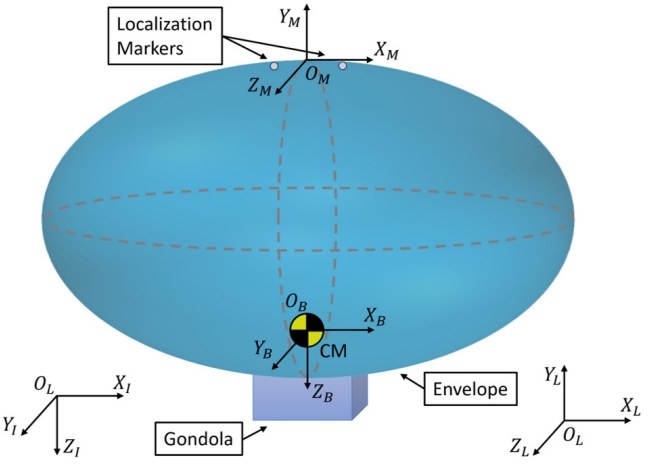


Fig. 12. Offset between the localization makers $O_M$, and the CM of GT-MAB.

Un. Sys. 2021.09:73-86. Downloaded from www.worldscientific.com
by CHINESE UNIVERSITY OF HONG KONG on 12/30/20. Re-use and distribution is strictly not permitted, except for Open Access articles.

Since the relationship between these two frames is already known, we have

$$
\begin{aligned}
{}^{M}_{B}\boldsymbol{R} &= \begin{bmatrix} 1 & 0 & 0 \\ 0 & 0 & -1 \\ 0 & 1 & 0 \end{bmatrix}, \\
{}^{M}_{B}\boldsymbol{q} &= [0, -H_{\mathrm{ENV}}/2, 0]^{\top}.
\end{aligned} \tag{29}
$$

Similarly, ${}^{M}\boldsymbol{p}_{\mathrm{CM}}$ can be represented in $O_L X_L Y_L Z_L$ as follows:

$$
{}^{L}\boldsymbol{p}_{\mathrm{CM}} = {}^{L}_{M}\boldsymbol{R}\,{}^{M}\boldsymbol{p}_{\mathrm{CM}} + {}^{L}_{M}\boldsymbol{q}, \tag{30}
$$

where ${}^{L}_{M}\boldsymbol{R}$ and ${}^{L}_{M}\boldsymbol{q}$ can be found as the attitude and position of the markers in the motion capture system. Then, the CM position in the inertial frame can be calculated as follows:

$$
{}^{I}\boldsymbol{p}_{\mathrm{CM}} = {}^{I}_{L}\boldsymbol{R}\,{}^{L}\boldsymbol{p}_{\mathrm{CM}} + {}^{I}_{L}q. \tag{31}
$$

With the relation between $O_L X_L Y_L Z_L$ and $O_I X_I Y_I Z_I$ defined in Sec. 2.1, we know that:

$$
\begin{aligned}
{}^{I}_{L}\boldsymbol{R} &= \begin{bmatrix} 1 & 0 & 0 \\ 0 & 0 & 1 \\ 0 & -1 & 0 \end{bmatrix}, \\
{}^{I}_{L}\boldsymbol{q} &= [0, 0, 0]^{\top}.
\end{aligned} \tag{32}
$$

Therefore, with the simplified notation $c\cdot = \cos(\cdot)$ and $s\cdot = \sin(\cdot)$, the CM position in inertia frame can be found as follows:

$$
{}^{I}\boldsymbol{p}_{\mathrm{CM}} = \begin{bmatrix} x_L + \left(\frac{H_{\mathrm{ENV}}}{2} + d_{\mathrm{VM}}\right)(c\phi_L s\psi_L - c\psi_L s\theta_L s\phi_L) \\ z_L - \left(\frac{H_{\mathrm{ENV}}}{2} + d_{\mathrm{VM}}\right) c\theta_L s\phi_L \\ -y_L + \left(\frac{H_{\mathrm{ENV}}}{2} + d_{\mathrm{VM}}\right)(c\phi_L c\psi_L + s\phi_L s\psi_L s\theta_L) \end{bmatrix}, \tag{33}
$$

where $[x_L, y_L, z_L]^{\top}$ and $[\phi_L, \theta_L, \psi_L]^{\top}$ are the position and Euler angles of the markers from the localization system.

### 4.4. *Feedback controller design*

Station keeping is one of the most common operating scenarios of GT-MAB. A flight controller is designed to keep GT-MAB at the desired position while simultaneously compensate the swing oscillation. As shown in Fig. 13, the proposed method consists of a station-keeping controller that tracks the position and heading of GT-MAB, and a swing-reducing controller which reduces the roll and pitch oscillation of the robot.

#### 4.4.1. *Station-keeping controller*

The station-keeping controller is an extension of our previous work [20]. The controller keeps GT-MAB at the desired position ${}^{I}\boldsymbol{p}_{\mathrm{ref}} = [{}^{I}x_{\mathrm{ref}}, {}^{I}y_{\mathrm{ref}}, {}^{I}z_{\mathrm{ref}}]^{\top}$, and holds its heading at $\psi_{\mathrm{ref}}$. As discussed in Sec. 4.3, the CM position of GT-MAB has significantly less fluctuation compared to that of the localization markers. Therefore, we use ${}^{I}\boldsymbol{p}_{\mathrm{CM}}$ to represent the position of GT-MAB. Hence, the distance and heading error can be calculated as follows:

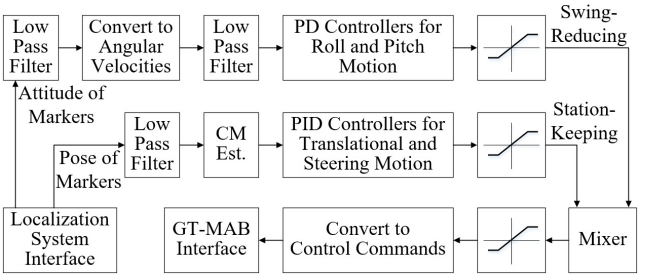


Fig. 13. Functional block diagram of the controller design.

$$
\begin{aligned}
{}^{I}\boldsymbol{e}_{\mathrm{pos}} &= {}^{I}\boldsymbol{p}_{\mathrm{ref}} - {}^{I}\boldsymbol{p}_{\mathrm{CM}}, \\
e_{\psi} &= \psi_{\mathrm{ref}} - \psi.
\end{aligned} \tag{34}
$$

Four PID controllers are implemented to minimize the position and the heading error. The controller outputs are denoted as $u_x, u_y, u_z$ and $u_{\psi}$, which can then be calculated separately by

$$
u_j = K_{p,j} e_j + K_{i,j} \int_0^t e_j dt' + K_{d,j} \frac{de_j}{dt}, \tag{35}
$$

where $j = \{x, y, z, \psi\}$. $u_j$ and $e_j$ denote the output and error of each controller. $K_{p,j}$, $K_{i,j}$, $K_{d,j}$ represent the PID gains of the individual controllers. The detailed modeling and control of the translational and steering motion of GT-MAB can be seen in [20].

Since the position errors are defined in the inertial frame, the controller outputs for the translational motion is then transferred to GT-MABs body frame as follows:

$$
[{}^{B}u_x, {}^{B}u_y, {}^{B}u_z]^{\top} = {}^{B}_{I}\boldsymbol{R}[u_x, u_y, u_z]^{\top}, \tag{36}
$$

where ${}^{B}_{I}\boldsymbol{R}$ is the rotation matrix between the inertia and body frame.

#### 4.4.2. *Swing-reducing controller*

The swing-reducing controller stabilizes the roll and pitch motion of GT-MAB during hovering flight. Given the roll and pitch dynamics of the blimp are decoupled and almost identical, we first design the controller for pitch motion, and then apply the same control law to stabilize both pitch and roll movement.

From the linearized model of the pitch motion described in Eq. (25), there are two poles in the open-loop dynamics. As shown in Fig. 14, the poles are located at $-0.0842 \pm 4.5190i$, indicating the open-loop dynamics is

Un. Sys. 2021.09:73-86. Downloaded from www.worldscientific.com
by CHINESE UNIVERSITY OF HONG KONG on 12/30/20. Re-use and distribution is strictly not permitted, except for Open Access articles.

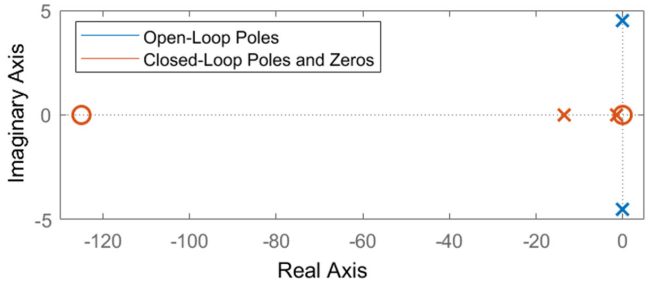


Fig. 14. Pole and zero plot of both open-loop and closed-loop dynamics of GT-MAB's pitch motion.

highly oscillatory with very limited damping. As a consequence, the undesired swing oscillation occurs once GT-MAB cannot damp the disturbance torque induced by its underactuated configuration. This issue becomes more significant when more powerful thrusters are installed for better maneuverability and flyability against airflow.

To reduce the oscillation of this stable but highly oscillatory system, a PD controller is designed to regulate the angular velocity of the pitch motion:

$$u_q = K_{p,q} e_q + K_{d,q} \frac{de_q}{dt}, \tag{37}$$

where $u_q$ and $e_q$ denote the output and angular rate error of the controller. $K_{p,q}$ and $K_{d,q}$ represent the PD gains separately.

As shown in Fig. 14, the closed-loop system under the PD controller has poles at –1.34 and –13.5 and zeros at 0 and –125. This indicates the closed-loop system has fast damping without oscillatory component.

The same control law is then applied to control the angular velocities of both pitch and roll motion, owing to the symmetrical design of GT-MAB. The setpoints of both controllers are set to zero for swing stabilization purpose. Therefore, the angular rate error of both controllers can be defined as follows:

$$e_{\text{swing}} = [e_p, e_q]^\top = [-p, -q]^\top, \tag{38}$$

where $p$ and $q$ are the angular velocities of GT-MAB around $X_B$ and $Y_B$ axes in the body frame. From Eq. (3), these angular rates can be found as follows:

$$\begin{aligned} p &= \dot{\phi} - \dot{\psi} \sin\theta, \\ q &= \dot{\theta} \cos\phi + \dot{\psi} \sin\phi \cos\theta, \end{aligned} \tag{39}$$

where $\phi$, $\theta$ and $\psi$ are the roll, pitch and yaw angles of GT-MAB. The outputs of the PD controllers are denoted as $u_p$ and $u_q$ for the roll and pitch motion separately. Since both $p$ and $q$ are already defined in GT-MABs body frame, the outputs can be written as follows:

$$\begin{aligned} {}^B u_p &= u_p, \\ {}^B u_q &= u_q. \end{aligned} \tag{40}$$

### 4.5. *Mixer design*

The outputs from both station-keeping and swing-reducing controllers are then mapped to the five gondola-mounted thrusters as shown in Fig. 15. The mixer is designed as follows:

$$\begin{bmatrix} f_1 \\ f_2 \\ f_3 \\ f_4 \\ f_5 \end{bmatrix} = \begin{bmatrix} \frac{1}{2} & 0 & 0 & 0 & \frac{1}{2d_{\text{MT1}}} & \frac{1}{d_{\text{SM}}} \\ \frac{1}{2} & 0 & 0 & 0 & \frac{1}{2d_{\text{MT2}}} & \frac{-1}{d_{\text{SM}}} \\ 0 & 0 & -\frac{1}{2} & 0 & 0 & 0 \\ 0 & 0 & -\frac{1}{2} & 0 & 0 & 0 \\ 0 & 1 & 0 & \frac{-1}{d_{MT5}} & 0 & 0 \end{bmatrix} \begin{bmatrix} {}^B u_x \\ {}^B u_y \\ {}^B u_z \\ {}^B u_p \\ {}^B u_q \\ {}^B u_\psi \end{bmatrix}, \tag{41}$$

where $f_1$–$f_5$ are the propulsion force generated by the thrusters as denoted in Fig. 15. $d_{\text{MT1}}$, $d_{\text{MT2}}$ and $d_{\text{MT5}}$ represent the distance between the CM and the thrusters with propulsion force $f_1$, $f_2$ and $f_5$ along $Z_B$ axis. $d_{\text{SM}}$ is the distance between the two surge motors with thrust force $f_1$ and $f_2$.

### 4.6. *Experimental results*

An experiment is designed to compare the proposed method to the traditional station-keeping controller without swing reduction feature. The experiment is conducted in an indoor laboratory with perturbations including air conditioning and air flow from human movement. Ten ceiling-mounted localization cameras (OptiTrack) capture the pose of GT-MAB at 120 Hz. The flight controllers and the ground-air communication also update at 120 Hz.

We first fly the blimp only with the station-keeping controller by disabling the swing-reducing feature. Thus the control outputs ${}^B u_p$ and ${}^B u_q$ are both zero. The setpoints of the station-keeping controller are set to ${}^I p_{\text{ref}} = [0, 0, 1.4]^\top$ and $\psi_{\text{ref}} = 0$ to keep GT-MAB hovering at the center of the indoor lab. As observed in Fig. 16, GT-MAB starts swinging

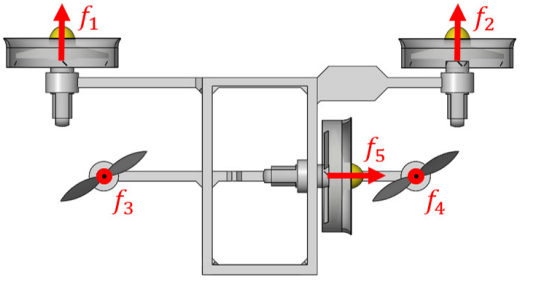


Fig. 15. Top view of GT-MABs gondola demonstrating the thruster configuration. Only the thrusters and the gondola frame are displayed for better illustration.

Un. Sys. 2021.09:73-86. Downloaded from www.worldscientific.com
by CHINESE UNIVERSITY OF HONG KONG on 12/30/20. Re-use and distribution is strictly not permitted, except for Open Access articles.

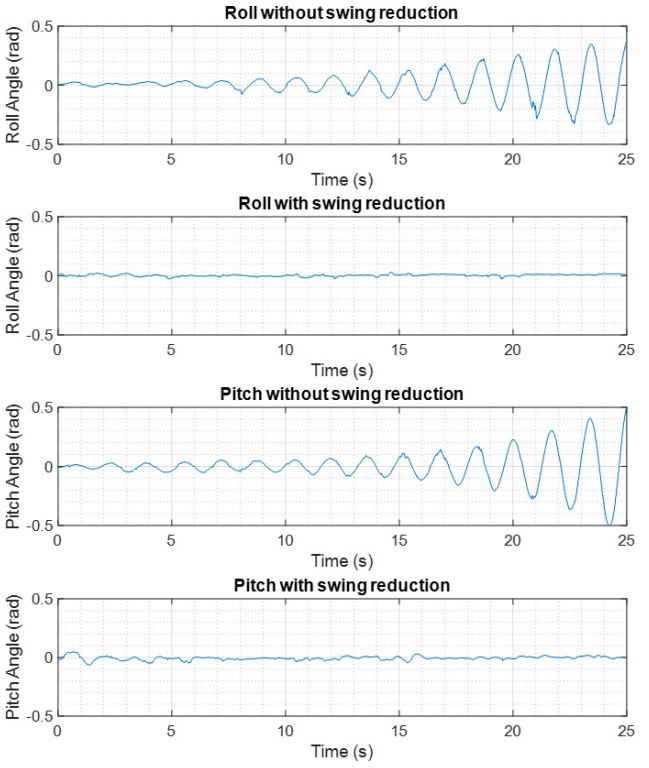


Fig. 16. Comparison of the roll and pitch angle of GT-MAB with and without swing-reducing controller.

severely within 20 s. As discussed in Sec. 4.4.2, this swing oscillation is due to the damping in roll and pitch dynamics is insufficient to cancel the undesired torque from the underactuated configuration of GT-MAB.

With the same experimental setup, we conduct the test with the swing-reducing controller engaged. Figure 16 compares the roll and pitch angle of GT-MAB with and without the swing stabilization controller during the first 25 s of flight. The figure demonstrates the swing oscillation of GT-MAB that is effectively stabilized after the swing-reducing controller is engaged. The variances of the roll and pitch angles of this flight test are also compared in Table 3.

Table 3. Variance of the roll and pitch angles of GT-MAB.

| Parameters | Without swing-reduction | With swing-reduction |
|---|---|---|
| Var. Roll (25 s) | 0.0133 rad$^2$ | 8.1502e-05 rad$^2$ |
| Var. Pitch (25 s) | 0.0174 rad$^2$ | 2.5425e-04 rad$^2$ |
| Var. Roll (Total of 347 s) | 0.0233 rad$^2$ | 5.5164e-04 rad$^2$ |
| Var. Pitch (Total of 1198 s) | 0.0271 rad$^2$ | 3.1007e-04 rad$^2$ |

The experiment is then repeated multiple times to further verify the purposed controller design. Ten un-stabilized tests with total flight time of 347 s, and three swing-stabilized tests with total of 1198 s are performed. As compared in Table 3, despite the increased environmental disturbances due to longer flight duration, the variances of both roll and pitch angles can be reduced by approximately two magnitudes with the engagement of the swing-reducing controller. A video demonstration of the flight test can be viewed at: https://youtu.be/d5UKV-dcpZg.

## 5. Conclusion and Future Work

This paper presents the modeling and control of the swing oscillation of GT-MAB, an underactuated indoor blimp. The dynamics of the swing motion is modeled, identified and linearized for controller design. The linearized model with identified parameters shows a satisfactory fit with the validation data. A swing-reducing flight control system is designed for the station-keeping mission with features including reduced latency and CM position estimation. Flight test results demonstrate that the flight control system can effectively reduce the swing oscillation of GT-MAB during the hovering flight.

We plan to expand the dynamic model of GT-MAB by incorporating the coupling between the translational and rotational motions. The flight control system will also be improved to reduce the swing oscillation while GT-MAB is in translational movement.

## Acknowledgments

The research work is supported by ONR Grant Nos. N00014-19-1-2556 and N00014-19-1-2266; AFOSR Grant No. FA9550-19-1-0283; NSF Grant Nos. CNS-1828678, S&AS-1849228 and GCR-1934836; NRL Grant Nos. N00173-17-1-G001 and N00173-19-P-1412; and NOAA Grant No. NA16NOS0120028.

## References

[1] D. Palossi, A. Gomez, S. Draskovic, A. Marongiu, L. Thiele and L. Benini, Extending the lifetime of nano-blimps via dynamic motor control, *J. Signal Process. Syst.* **91**(3–4) (2018) 339–361.

[2] Z. Fang and S. Scherer, Real-time onboard 6dof localization of an indoor mav in degraded visual environments using a rgb-d camera, *2015 IEEE Int. Conf. Robotics and Automation (ICRA)*2015, pp. 5253–5259.

[3] K. Asadi, A. K. Suresh, A. Ender, S. Gotad, S. Maniyar, S. Anand, M. Noghabaei, K. Han, E. Lobaton and T. Wu, An integrated ugv-uav system for construction site data collection, *Autom. Construct.* **112** (2020) 103068.

[4] Y. Wang, G. Zheng, D. Efimov and W. Perruquetti, Disturbance compensation based controller for an indoor blimp robot, *Robot. Auton. Syst.* **124** (2020) 103402.

Un. Sys. 2021.09:73-86. Downloaded from www.worldscientific.com
by CHINESE UNIVERSITY OF HONG KONG on 12/30/20. Re-use and distribution is strictly not permitted, except for Open Access articles.

[5] D. St-Onge, P. Brches, I. Sharf, N. Reeves, I. Rekleitis, P. Abouzakhm, Y. Girdhar, A. Harmat, G. Dudek and P. Gigure, Control, localization and human interaction with an autonomous lighter-than-air performer, *Robot. Auton. Syst.* **88** (2017) 165–186.

[6] R. A. S. Fernndez, J. L. Sanchez-Lopez, C. Sampedro, H. Bavle, M. Molina and P. Campoy, Natural user interfaces for human-drone multi-modal interaction, *2016 Int. Conf. Unmanned Aircraft Systems (ICUAS)*, 2016, pp. 1013–1022.

[7] S. Hwan Song, H. Wook Shon, G. Yang Yeon and H. Ryeol Choi, Design and implementation of cloud-like soft drone s-cloud, *2018 IEEE/RSJ Int. Conf. Intelligent Robots and Systems (IROS)*, 2018, pp. 1–9.

[8] V. Srisamosorn, N. Kuwahara, A. Yamashita, T. Ogata, S. Shirafuji and J. Ota, Indoor human face following with environmental fisheye cameras and blimp, *Adv. Robot.* **34** (2020) 621–636.

[9] N. Yao, E. Anaya, Q. Tao, S. Cho, H. Zheng and F. Zhang, Monocular vision-based human following on miniature robotic blimp, *IEEE Int. Conf. Robot. Autom. (ICRA)* 2017, pp. 3244–3249.

[10] S. U. Ferdous, A. Mohammadi and S. Lakshmanan, Developing a low-cost autonomous blimp with a reduced number of actuators, *Unmanned Syst. Technol. XXI* Vol. 11021 (SPIE, 2019), pp. 73–80.

[11] W. Yamada, H. Manabe and D. Ikeda, Zerone: Safety drone with blade-free propulsion, in *Proc. 2019 CHI Conf. Human Factors in Computing Systems*, 2019, pp. 1–8.

[12] B. Siciliano and O. Khatib*Springer Handbook of Robotics* (Springer-Verlag, Berlin, 2016).

[13] Y. Bestaoui-Sebbane, *Lighter than Air Robots* (Springer, Netherlands, 2012).

[14] C. Blouin, E. Lanteigne and W. Gueaieb, Optimal control for the trajectory planning of micro airships, *2017 Int. Conf. Unmanned Aircraft Systems (ICUAS)* 2017, pp. 885–892.

[15] R. Saitou, Y. Ikeda and Y. Oikawa, Three-dimensional noise and spatial mapping system with aerial blimp robot, *Acoust. Sci. Technol.* **40**(1) (2019) 12–22.

[16] T. Takaya, H. Kawamura, Y. Minagawa, M. Yamamoto and A. Ohuchi, Pid landing orbit motion controller for an indoor blimp robot, *Artif. Life Robot.* **10**(2) (2006) 177–184.

[17] F. Zhang, Q. Tao, T. Tan, P. Cheng, S. Cho, V. Mishra and J. Varnell, Miniature autonomous robotic blimp, US patent application 16/280,579 (2019).

[18] N. Yao, Q. Tao, W. Liu, Z. Liu, Y. Tian, P. Wang, T. Li and F. Zhang, Autonomous flying blimp interaction with human in an indoor space, *Front. Inf. Tech. Electron. Eng.* **20**(1) (2019) 45–59.

[19] Q. Tao, M. King-Smith, A. Muni, V. Mishra, S. Cho, P. Varnell and F. Zhang, Control theory - autonomous blimp, *IEEE CSS Video Clip Contest*, 2015.

[20] S. Cho, V. Mishra, Q. Tao, P. Varnell, M. King-Smith, A. Muni, W. Smallwood and F. Zhang, Autopilot design for a class of miniature autonomous blimps, in *Proc. of IEEE Conf. Control Technol. Appl. (CCTA)*, 2017, pp. 841–846.

[21] G. Lu and F. Zhang, Imu-based attitude estimation in the presence of narrow-band noise, *IEEE/ASME Trans. Mechatron.* **24**(2) (2019) 841–852.

[22] Y. Li, M. Nahon and I. Sharf, Airship dynamics modeling: A literature review, *Prog. Aerospace Sci.* **47**(3) (2011) 217–239.

[23] Z. Ashraf and M. A. Choudhry, Dynamic modeling of the airship using analytical aerodynamic model, *2009 Int. Conf. Emerging Technol.* 2009, pp. 188–193.

[24] M. D. Reddy and R. S. Pant, Cfd analysis of axisymmetric bodies of revolution using openfoam, *2018 Appl. Aerodyn. Conf.*, 2018, p. 10.

[25] J. L. M. Junior, J. S. Santos, M. A. Morales, L. C. Goes, S. Stevanovic and R. A. Santana, Airship aerodynamic coefficients estimation based on computational method for preliminary design, *AIAA Aviation 2019 Forum*, 2019.

[26] S. B. V. Gomes and J. G. Ramos, Airship dynamic modeling for autonomous operation, *Pro. IEEE Int. Conf. Robotics and Automation*, Vol. 4 (1998), pp. 3462–3467.

[27] J. Shan, Dynamic modeling and vision-based control for indoor airship, in *Int. Conf. Mechatronics and Automation*, 2009, pp. 2934–2939.

[28] J.-C. Zufferey, A. Guanella, A. Beyeler and D. Floreano, Flying over the reality gap: From simulated to real indoor airships, *Auton. Robot.* **21**(3) (2006) 243–254.

[29] F. Hayato and S. Akira, Wind-disturbance-based control approach for blimp robots, *Electron. Commun. J.* **97**(2) (2014) 52–59.

[30] C. Wan, N. Kingry and R. Dai, Design and autonomous control of a solar-power blimp, in *2018 AIAA Guidance, Navigation, and Control Conf. AIAA SciTech Forum*, 2018, p. 1588.

[31] S. Kale, P. Joshi and R. Pant, A generic methodology for determination of drag coefficient of an aerostat envelope using cfd, in *AIAA 5th ATIO and 16th Lighter-Than-Air Sys Tech. and Balloon Syst. Conf.* 2005, p. 7442.

[32] Y. Wang, G. Zheng, D. Efimov and W. Perruquetti, Altitude control for an indoor blimp robot, *IFAC-PapersOnLine* **50**(1) (2017) 15990–15995, 20th IFAC World Congress.

[33] Q. Tao, J. Cha, M. Hou and F. Zhang, Parameter identification of blimp dynamics through swinging motion, *2018 15th Int. Conf. Control, Automation, Robotics and Vision (ICARCV)*, 2018, pp. 1186–1191.

[34] V. Srisamosorn, N. Kuwahara, A. Yamashita, T. Ogata and J. Ota, Design of face tracking system using fixed 360-degree cameras and flying blimp for health care evaluation, in *4th Int. Conf. Serviceology*, 2016, pp. 63–66.

[35] D. Palossi, Self-sustainability in nano unmanned aerial vehicles: A blimp case study, in *CF'17 Proc. Computing Frontiers Conf.* 2017, pp. 79–88.

[36] N. Wang, H. R. Karimi, H. Li and S. Su, Accurate trajectory tracking of disturbed surface vehicles: A finite-time control approach, *IEEE/ASME Trans. Mechatron.* **24**(3) (2019) 1064–1074.

[37] N. Wang and H. R. Karimi, Successive waypoints tracking of an underactuated surface vehicle, *IEEE Trans. Ind. Inform.* **16**(2) (2020) 898–908.

[38] P. Gonzalez, W. Burgard, R. Sanz and J. L. Fernandez, Developing a low-cost autonomous indoor blimp, *J. Phys. Agents* (2009) 43–52.

[39] S. B. I. Badia, P. Pyk and P. F. M. J. Verschure, A biologically based flight control system for a blimp-based uav, in *Proc. 2005 IEEE Int. Conf. Robotics and Automation*, 2005, pp. 3053–3059.

[40] T. Takaya, H. Kawamura, Y. Minagawa, M. Yamamoto and A. Ouchi, Motion control in three dimensional round system of blimp robot, in *2006 SICE-ICASE Int. Joint Conf.* 2006, pp. 1291–1294.

[41] H. Kawamura, M. Yamamoto, T. Takaya and A. Ohuchi, Learning landing control of an indoor blimp robot for self-energy recharging, *Artif. Life Robot.* **12**(1) (2008) 116–121.

[42] H. Kawamura, H. Iizuka, T. Takaya and A. Ohuchi, Cooperative control of multiple neural networks for an indoor blimp robot, *Artif. Life and Robot.* **13**(2) (2009) 504–507.

[43] M. Mahn and M. Kemper, A behaviour-based navigation system for an autonomous indoor blimp, *IFAC Proc. Vol.* **39**(16) (2006) 837–842, 4th IFAC Symp. Mechatron. Syst.

[44] Y. Wang, G. Zheng, D. Efimov and W. Perruquetti, Improved altitude control method with disturbance compensation for an indoor blimp robot, *2017 IEEE 56th Annual Conf. Decision and Control (CDC)* 2017, pp. 3902–3907.

[45] Y. Wang, G. Zheng, D. Efimov and W. Perruquetti, Differentiator application in altitude control for an indoor blimp robot, *Int. J. Control* **91**(9) (2018) 2121–2130.

[46] J. Gibson, T. Schuler, L. McGuire, D. M. Lofaro and D. Sofge, Swarm and multi-agent time-based a* path planning for lta3 systems, *Unmanned Syst.* **8**(3) (2020) 253–260.

[47] K. Watanabe, N. Okamura and I. Nagai, Closed-loop control experiments for a blimp robot consisting of four-divided envelopes, *IECON 2015 - 41st Annual Conf. IEEE Industrial Electronics Society*, 2015, pp. 002568–002573.
[48] I. M. Mladenov, On the geometry of the mylar balloon, *Comptes Rendus de l'Academie Bulgare des*, **54** (2001) 9–39.
[49] About mass properties Autodesk Knowledge Network (Accessed: 28 June 2018).
[50] L. Ljung, *System Identification Toolbox User's Guide*. MathWorks, Inc, 3 Apple Hill Drive Natick, MA 01760-2098 (2018).
[51] V. Lchapp, S. Rouquet, A. Gonzlez, F. Plestan, J. D. Len, E. Moulay and A. Glumineau, Delay estimation and predictive control of uncertain systems with input delay: Application to a dc motor, *IEEE Trans. Ind. Electron.* **63**(9) (2016) 5849–5857.

Un. Sys. 2021.09:73-86. Downloaded from www.worldscientific.com
by CHINESE UNIVERSITY OF HONG KONG on 12/30/20. Re-use and distribution is strictly not permitted, except for Open Access articles.

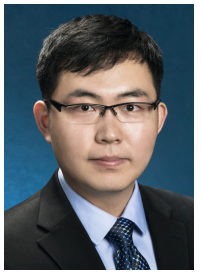

**Qiuyang Tao** received the B.S. in Electrical Engineering from the Georgia Institute of Technology, Atlanta GA, USA, in 2015. He is continuing his Ph.D. studies in Electrical and Computer Engineering at the Georgia Institute of Technology. Qiuyang's current research interests include the design, modeling and control of novel robotic and mechatronic systems.

**Tun Jian Tan** is receiving his B. Eng. in Computer Engineering in 2020 from the Hong Kong University of Science and Technology. His current research interests include unmanned aerial vehicle and computer vision for robotics.

**Jaeseok Cha** received the B.S. and M.S. degrees in Mechanical Engineering from Georgia Institute of Technology, Atlanta, GA, USA, in 2017 and 2018, respectively. He is currently a research engineer with Hyundai Mobis, Yongin, South Korea. His current research interests include perceptions of advanced driver assistance systems.

**Ye Yuan** received the B. Eng. degree (Valedictorian) from the Department of Automation, Shanghai Jiao Tong University, Shanghai, China, in 2008, and the M.Phil. and Ph.D. degrees from the Department of Engineering, University of Cambridge, Cambridge, U.K., in 2009 and 2012, respectively. He has been a Full Professor at the Huazhong University of Science and Technology, Wuhan, China since 2016. Prior to this, he was a Postdoctoral Researcher at UC Berkeley, a Junior Research Fellow at Darwin College, University of Cambridge. His research interests include system identification and control with applications to cyber-physical systems. Dr. Yuan has received the China National Recruitment Program of 1000 Talented Young Scholars, the Dorothy Hodgkin Postgraduate Awards, Microsoft Research Ph.D. Scholarship, Best of the Best Paper Award at the IEEE Power and Energy Society General Meeting.

**Fumin Zhang** received the B.S. and M.S. degrees from Tsinghua University, Beijing, China, in 1995 and 1998, respectively, and the Ph.D. degree from the Department of Electrical and Computer Engineering, University of Maryland, College Park, in 2004. He joined the School of ECE, Georgia Institute of Technology in 2007, where he is a Professor. He was a Lecturer and Postdoctoral Research Associate in the Mechanical and Aerospace Engineering Department, Princeton University from 2004 to 2007. His research interests include marine autonomy, mobile sensor networks and theoretical foundations for battery supported cyber-physical systems. He received the NSF CAREER Award in 2009 and the ONR YIP Award in 2010.